Diffusion MRI Detects Early Brain Microstructure Abnormalities in 2-month-old 3xTg-AD Mice

Maria Fatima Falangola[1,2,a], **Xingju Nie**[1,2,a], **Ralph Ward**[4], **Emilie T. McKinnon**[1,3], **Siddhartha Dhiman**[1], **Paul J. Nietert**[4], **Joseph A. Helpern**[1,2], **Jens H. Jensen**[1,2,5]

[1]Department of Neuroscience, Medical University of South Carolina, Charleston, South Carolina, USA

[2]Center for Biomedical Imaging, Medical University of South Carolina, Charleston, South Carolina, USA

[3]Department of Neurology, Medical University of South Carolina, Charleston, South Carolina, USA

[4]Department of Public Health Sciences, Medical University of South Carolina, Charleston, SC, USA

[5]Department of Radiology and Radiological Science, Medical University of South Carolina, Charleston, South Carolina, USA

SUMMARY

The 3xTg-AD mouse is one of the most studied animal modes of AD, and develops both amyloid-β deposits and neurofibrillary tangles in a temporal and spatial pattern that is similar to human AD pathology. Additionally, abnormal myelination patterns with changes in oligodendrocyte and myelin marker expression are reported to be an early pathological feature in this model. Only few diffusion MRI (dMRI) studies have investigated white matter (WM) abnormalities in 3xTg-AD mice, with inconsistent results. Thus, the goal of this study was to investigate the sensitivity of dMRI to capture brain microstructural alterations in 2-month-old 3xTg-AD mice. In the fimbria, the fractional anisotropy (FA), kurtosis fractional anisotropy (KFA), and radial kurtosis (K⊥) were found to be significantly lower in 3xTg-AD mice than in controls, while the mean diffusivity (MD) and radial diffusivity (D⊥) were found to be elevated. In the fornix, K⊥ was lower for 3xTg-AD mice; in the dorsal hippocampus MD and D⊥ were elevated, as were FA, MD, and D⊥ in the ventral hippocampus. These results indicate, for the first time, dMRI changes, associated with myelin abnormalities in young 3xTg-AD mice, before they develop AD pathology. Morphological quantification of myelin basic protein MBP immunoreactivity in the fimbria was significantly lower in the 3xTg-AD mice compared to the NC. Our results demonstrate that dMRI is able to detect widespread, significant early brain morphological abnormalities in 2-month-old 3xTg-AD mice.

Corresponding author: Dr. Maria de Fatima Falangola, Department of Neuroscience & Center for Biomedical Imaging, Medical University of South Carolina, 68 President St, Bioengineering Building Rm 207, Charleston SC 29425-0120, Office phone: 843-876-2466, falangol@musc.edu.
(a)These authors contributed equally to the work.

Graphical Abstract
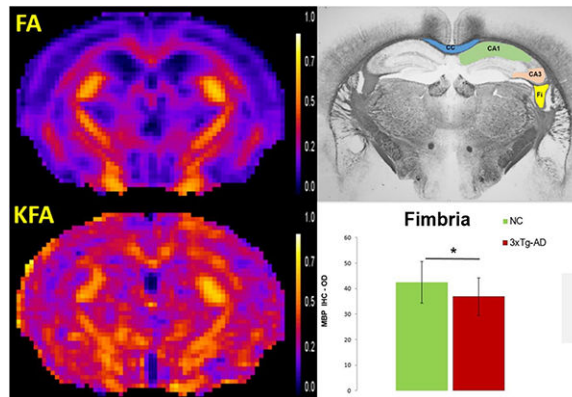
In vivo diffusion MRI metrics are shown to be sensitive indicators of early changes in the integrity and complexity of the white matter (WM) microstructure in 2 months-old 3xTg-AD mice. Widespread significant WM abnormalities were detected and supported by histological (myelin basic protein immunohistochemistry) findings.

Keywords

Diffusion MRI; Diffusional kurtosis imaging; 3xTg-AD mouse; White matter; Alzheimer's disease

1. Introduction

Alzheimer's disease (AD) pathology is remarkably heterogeneous and complex. The pathologic hallmarks are the accumulation of amyloid-β (Aβ) and its aggregation into fibrillar plaques, as well as the hyperphosphorylation of tau protein, resulting in intracellular neurofibrillary tangles[1,2]. Additionally, decrease in synaptic density, neuronal loss, neuro-inflammation, impaired glucose metabolism, and white matter (WM) disruption are all essential features of the pathological process[3–7]. However, it is still unclear what brain morphological changes exist prior to the full onset of AD-related pathology and cognitive changes, and no effective diagnostic biomarkers for early features of AD exists.

The need to identify mechanisms of disease, diagnostic biomarkers and therapeutic tools for AD has led to the development of several transgenic mouse models of AD[8,9]. One of the most studied of these is the triple transgenic mouse model of AD (3xTg-AD). The 3xTg-AD model possesses the three mutations of human presenilin-1 M146V, human amyloid precursor protein Swedish mutation, and the P301L mutation of human tau, based on human mutations identified in familial AD[10]. It develops both Aβ and neurofibrillary tangles (NFTs) in a temporal and spatial pattern that is similar to human AD pathology[11–13]. In this model, intraneuronal Aβ begins to accumulate around 2 months of age, while extracellular Aβ deposits are apparent by 6 months, particularly in the caudal hippocampus, and become more extensive by twelve months[14]. These mice exhibit synaptic plasticity dysfunction, including long-term potentiation (LTP) deficits that occur prior to extracellular Aβ

deposition, but are associated with intracellular Aβ[13]. Cognitive impairment manifests at 3–4 months of age, correlating both with the accumulation of soluble and intraneuronal Aβ in the hippocampus and amygdala[15] and with altered synaptic plasticity[16]. Neuro-inflammation is present starting around 6 months of age when reactive microglia are detected in the hippocampus, and later with increased pathology, activated astrocytes appear around Aβ plaques[14]. This model also develops tau pathology that begins around 6 months, when phosphorylated tau becomes detectable in the caudal hippocampus, and develops into neurofibrillary tangles after 12 months of age[13,14].

These observations in 3xTg-AD mice show that physiological and behavioral changes are present at an early age, even before amyloid and tau-related pathologies are observed. Interestingly, abnormal myelination patterns with changes in oligodendrocyte and myelin marker expression are reported to be the first pathological feature described in the 3xTg-AD mice, leading to WM disruption in the hippocampus and entorhinal cortex as early as 2 months of age[17,18]. These WM changes are followed by the first signs of cognitive impairment, detected even before Aβ plaques appear[18]. Therefore, the 3xTg-AD mice exhibit an essential feature, WM disruption earlier in the pathological process, which can provide valuable insight into a possible early pathological mechanism of AD and help identify biomarkers for early detection.

Diffusion MRI (dMRI) is a powerful method for probing brain microstructure abnormalities and is widely used as a noninvasive tool for detecting changes in age- and AD-associated WM integrity[19,20]. Diffusional kurtosis imaging (DKI) is a specific dMRI technique that extends diffusion tensor imaging (DTI) by quantifying the non-Gaussian behavior of water diffusion, contributing additional information beyond that provided by DTI[21–23]. Despite the well characterized morphological and histochemical WM abnormalities in the 3xTg-AD mouse model, few dMRI studies have investigated WM abnormalities in this model. Employing DTI, Kastyak-Ibrahim et al.[24] reported no WM differences in older (11–17 months of age) 3xTg-AD mice relative to controls, whereas our group, using DKI[25], demonstrated that WM microstructure changes can be detected longitudinally with dMRI, particularly in the fimbria and external capsule of 3xTg-AD mice (4.5 to 18 months of age). Recently, Manno et al.[26] reported significant fractional anisotropy increase and radial diffusivity decrease in the cortex of 2-month-old 3xTg-AD mice compared with controls. We also recently reported, in a small sample of mice (3xTg-AD, n = 14; NC, n = 8), statistically significant dMRI changes in the hippocampus and fimbria of 3xTg-AD mice, illustrating that dMRI metrics can detect early pathological features in this AD mouse model[27]. Moreover, two more structural MRI studies have reported significant volumetric differences in the hippocampus and several WM regions, including fimbria, in young 3xTg-AD mice[28,29].

These results warrant further studies with this model on the potential of MRI, particularly dMRI, as a tool for detecting early AD pathology. Thus, the goal of this study was to further investigate the sensitivity of dMRI to capture brain microstructural alterations associated with the hippocampus and fimbria-fornix circuit in 2-month-old 3xTg-AD mice.

2. Methods

2.1 AD mouse model

All experimental procedures were approved by the Institutional Animal Care and Use Committee at the Medical University of South Carolina (MUSC), and conducted in accordance with the National Institutes of Health (NIH) Guide for Care and Use of Laboratory Animals. All animals were purchased from *The Jackson Laboratory*. The 3xTg-AD (n = 59) [B6;129-Psen1tm1Mpm Tg(APPSwe, tauP301L)1Lfa/Mmjax; MMRRC Stock No: 34830-JAX|3xTg-AD] and age-matched controls (NC, n = 41) [101045 B6129SF2/J] were studied at 2 months of age. The control mice for the 3xTg-AD are the suggested controls for genetically engineered strains generated with 129-derived embryonic stem cells and maintained on a mixed B6;129 background. Only 2-month-old female mice were used in this study since the development of AD pathology is far less pronounced and more variable in male 3xTg-AD mice[14,30]. All mice were housed in temperature- and humidity-controlled rooms on a 12-h light/dark cycle (lights on at 6:00 AM) in an accredited animal care facility.

2.2 MRI acquisition

Mice were anesthetized using an isoflurane vaporizer set at the following percentages: 3% for induction, 2% during pilot scanning and data acquisition. An animal monitoring unit (SA instruments, Inc., model 1025, Stony Brook, NY) was used to record respiration and rectal temperature. Respiration was measured with a pressure transducer placed under the abdomen just below the ribcage. Body temperature was maintained using ventilated warm air, controlled by a feedback circuit between the heater and thermistor. After induction, mice were placed on a mouse holder and restrained using a mouse tooth bar (Bruker, T10146) and ear bars (Bruker, T10147) placed in the auditory canal. Compressed air was used as the carrier gas and delivered at a flow rate of 1L/min to a nose cone positioned around the tooth bar, where gases mixed with air and passed over the rodent's nose. All animals were maintained at $37.0 \pm 0.2°C$ and respiration ranged between 60 and 80 breaths per minute during scanning.

The *in vivo* MRI experiments were all performed on a 7T Bruker Biospin 30 cm bore scanner (BioSpec 70/30 USR) running Paravision version 5.1. This system is equipped with a 12 cm high performance B-GA 12S2 gradient and shim coil set, capable of generating a maximum gradient amplitude of 440 mT/m and a slew rate of 4570 T/m/s. A 86 mm 1H quadrature volume coil (T128038) was used for signal transmission and an actively decoupled phase array coil (four channel receiver T11765) was used for signal reception. A 2-shot SE-EPI dMRI sequence was employed for the DKI acquisition[21,22]. The main imaging parameters were: TR/TE = 3750/32.6 ms, δ/ = 5/18ms, slice thickness = 0.7 mm, 15 slices with no gap, data matrix = 128×128, image resolution = 156×156 μm^2, 2 signal acquisitions, 10 b-value = 0 (b0) images, followed by 30 diffusion encoding gradient directions with 4 b-values for each gradient direction (0.5, 1.0, 1.5, and 2.0 ms/μm^2) and fat suppression flip angle = 105°. Total acquisition time = 33 minutes.

2.3 DKI post-processing and Image analysis

DKI post-processing was performed using DKE[31] (http://nitrc.org/projects/dke). Post-processing included motion correction by aligning all DWIs to the first b=0 image using SPM12 (Wellcome Trust Centre for Neuroimaging, UCL, UK). A principal component analysis approach[32] and the method of moments[33] were used to reduce the effects of signal noise on the dMRI data. An example of the dMRI raw data for one slice and all b-values at 3 diffusion directions is presented in the Supplementary Figure 1. Parametric maps were obtained by fitting dMRI signal measurements to the DKI signal model for each voxel using a linearly constrained weighted linear least squares fitting algorithm, which generated the diffusion and kurtosis tensors. These two tensors were then used to calculate parametric maps for all diffusion metrics[22,23]. Figure 1 illustrates the slice selection and maps for all diffusion metrics for both NC and 3xTg-AD mice. In our analysis, we considered the four diffusion tensor (DT) parameters of mean diffusivity (MD), axial diffusivity ($D_\parallel$), radial diffusivity ($D_\perp$), and fractional anisotropy (FA). MD corresponds to the diffusivity averaged over all diffusion directions, $D_\parallel$ corresponds to the diffusivity in the direction of the principal diffusion tensor eigenvector, $D_\perp$ corresponds to the diffusivity averaged over all diffusion directions perpendicular to the principal diffusion tensor eigenvector, and FA quantifies the anisotropy of the diffusion tensor. We similarly considered the four diffusional kurtosis (DK) metrics of mean kurtosis (MK), axial kurtosis ($K_\parallel$), radial kurtosis($K_\perp$), and kurtosis fractional anisotropy (KFA). These are kurtosis analogs of the DT metrics that quantify diffusional non-Gaussianity and provide complementary information about the diffusion dynamics[23,34]. All four b-values (0.5, 1.0, 1.5, 2.0 ms/μm^2), for each gradient direction, were used in calculating the diffusion metrics. It is worth noting that, due to the inclusion of non-Gaussian effects, DKI yields more accurate estimates of DT metrics than does conventional DTI[35], as well as enabling a more comprehensive assessment of the diffusion microenvironment in brain tissue.

Regions of interest (ROIs) were defined for dorsal (DH - two slices) and ventral (VH - two slices) hippocampus, fimbria (Fi - three slices) and fornix (Fx - one slice). Additionally, we assessed corpus callosum (CC - five slices), external (EC - five slices) and internal (IC - two slices) capsule, which are WM tracks relevant to age-related changes and AD pathology. All ROIs were manually drawn on the averaged b0 image by a neuropathologist (MFF), using ImageJ (http://imagej.nih.gov/ij//)[36]. Anatomical guidelines for outlining these regions were determined by comparing anatomical structures in the MRI slices with a standard mouse atlas[37] and verified with the FA maps to ensure correct anatomical location and to avoid contamination of unintended tissue or cerebrospinal fluid (CSF). To reduce bias when drawing the ROIs, we randomly chose mice ID numbers, which included both NC and 3xTg-AD mice, and sampled the same number of MRI slices for each mouse for each ROI. To test for inconsistencies in ROI delineation, we investigated the size of ROIs for bias towards any group. We found no statistical differences, except in the hippocampus, where 3xTg-AD mice had a small number of voxels sampled (Supplementary Table 1), which is likely related to the small hippocampus volume previously described for this strain[28,29]. Figure 2 shows FA maps for a 3xTg-AD mouse with the selected ROIs drawn. The regional values for the dMRI measures were obtained by averaging all voxels within an ROI except

those with MD $^>$ 1.5 μm^2/ms, which were excluded to minimize the effect of CSF contamination.

2.4 Histological protocol

Following the MRI scan, a subset of mice from each group (3xTg-AD, n = 9; NC, n = 5) were perfused with ice-cold phosphate buffered saline (PBS) followed by paraformaldehyde (4%) in PBS. Mice brains were then removed and post-fixed overnight in the same fixative, and subsequently transferred to a storage buffer PBS with 0.02% sodium azide until final processing by NeuroScience Associates (Knoxville, TN, USA) using MultiBrain® technology. Brains were freeze-sectioned at 25 μm in the coronal plane and two consecutive sections at the level of the dorsal hippocampus (Bregma −2.00 mm, based on the mouse brain atlas[37]) were stained free-floating with myelin basic protein (MBP; Abcam ab40390, Cambridge, MA, USA) to measure the degree of myelination. The two slices were digitized in one session using an Olympus BX53 microscope with QImaging digital camera and QCapture Suite. Images (4x magnification) were acquired under the same image light and camera settings to avoid possible image intensity variation, and then saved as 8-bit grayscale images.

All ROIs were manually drawn by a neuropathologist (MFF) on the two consecutive digital images in both hemispheres, resulting in 20 measurements for NC mice and 33 measurements for 3xTg-AD taking into account some histological tissue damage in a few of the 3xTg-AD mice. ROIs were drawn, based on the mouse brain atlas[37], at the level of fimbria (Fi), corpus callosum (CC) and dorsal hippocampus (CA1 and CA3 regions) using ImageJ software (Figure 3A). The quantification of the MBP immunoreactivity was done by averaging the mean grayscale intensity measurements from all pixels in each ROI, and values were expressed as optical density (OD) = log (max intensity/mean intensity), where max intensity = 255 for the 8-bit images.

2.5 Statistical analyses

All data is expressed as group averaged means ± standard deviation of the mean (SD). For both the morphological and dMRI values, two-tailed, two-sample t-tests were performed to assess differences in the measurements between the two groups for each ROI. Also, the effect size (Cohen's d) was determined to assess the magnitude of the differences between the two groups. Additionally, for the dMRI values, a Bonferroni correction was applied to explore which group differences would remain significant after correcting for multiple comparisons (8 dMRI metrics compared within each ROI). Finally, we also determined the percentage differences between the two groups (% Difference = ($Mean_{3xTg-AD}$ − $Mean_{NC}$) / $Mean_{NC}$ * 100%) for each dMRI metric for each ROI. An adjusted p-value of 0.05 was considered to be statistically significant (which corresponds to an unadjusted p-value 0.00625). Analyses were conducted using SAS v9.4 (SAS Institute, Cary, NC).

3. Results

Tables 1 and 2 give the group means, standard deviations, unadjusted p-values (bold indicates values that remain significant after Bonferroni correction), Cohen's d, and the

percentage differences for the for the DT and DK metrics from all ROIs. Boxplots for the DT and DK metrics in each ROI are seen in Figure 4 and 5, respectively.

Our results show that dMRI metrics are able to capture brain tissue microstructural differences between the two groups, even at this young age. The Fi had a significantly lower FA, KFA, and $K\perp$ for the 3xTg-AD group than for the NC group, while the MD and $D\perp$ were higher for the 3xTg-AD mice. In this region, most of the significant metrics had a large Cohen's d value, but $D\perp$ showed the most sensitivity between groups with respect to yielding a statistically significant p value, a larger Cohen's d value and the largest percentage difference. In the Fx, $K\perp$ was significantly lower in the AD mice, but the effect size and percentage difference were moderate. In the CC of the 3xTg-AD mice, FA, $D_{\parallel}$, KFA, MK and $K\perp$, were significantly lower, while $D\perp$ was significantly higher compared to controls. In this region, FA and $K\perp$ were the most sensitive to differentiate between the two groups, with larger Cohen's d values and percentage differences. MK and $K\perp$ were significantly lower in the IC of the 3xTg-AD mice, and the magnitude of the differences was large. MK was also significantly lower in the EC of these mice compared with NC, with a medium effect size. In the DH of the 3xTg-AD mice, MD and $D\perp$ were significantly higher than for the NC group, with larger effect sizes. In the VH of these mice FA, MD and $D_{\parallel}$ were significantly higher compared with NC, with FA and $D_{\parallel}$ having the larger Cohen's d values.

Morphological quantification of MBP immunoreactivity in the Fi was significantly lower (p= 0.014; d= −0.719) in the 3xTg-AD mice compared to the NC, but no differences were detected in the CC, CA1 or CA3 regions (Figure 3 B, C, D; Supplementary Table 2). No correlations between morphological data and dMRI metrics were detected in any of the regions investigated (data not shown).

4. Discussion

Our results demonstrate that dMRI is able to detect brain morphological abnormalities in young 3xTg-AD mice for multiple brain regions. Our findings of lower FA, KFA, and $K\perp$, and elevated MD and $D\perp$ in the Fi, together with significantly lower $K\perp$ in the Fx and significantly higher diffusivity metrics at the level of dorsal (MD and $D\perp$) and ventral hippocampus (FA, MD and $D_{\parallel}$), indicate WM disruption in the hippocampus-fimbria-fornix circuit in the 3xTg-AD mice.

This is consistent with previously described morphological changes where abnormal oligodendrocyte and myelin marker expression are noticeable in the hippocampus of 2-month-old 3xTg-AD mice[17,18], as well as with our own histological measurement of myelin immunoreactivity in the Fi. Although there was a trend for MBP decrease in the corpus callosum and CA3 of the 3xTg-AD mice, it did not reach significance (Figure 3D). Probably the small subset of mice used in the morphological analysis hindered our ability to detect differences in MBP immunoreactivity in other brain regions other than fimbria. Therefore, a more detailed morphological characterization in this model is needed to establish a direct correlation between dMRI and morphology findings.

The efferent fibers of the hippocampus are collected together in the fimbria and fornix forming a complex system of fibers closely related functionally and structurally with the hippocampal formation. Significant volumetric differences across the entire brain, particularly changes in the structural integrity of the hippocampal complex and fimbria have been reported in young 3xTg-AD mice[28,29], which together with myelin abnormalities, may be the contributing factors to the dMRI changes detected in our study. Similarly, previous human studies have demonstrated that fornix and fimbria abnormalities are detectable at an early stage of AD pathogenesis, with associations between disrupted microstructure and worse memory performance in healthy adults, as well as in older adults with MCI and AD dementia[38–44]. Additionally, some studies have observed a significant relationship between reduced microstructural integrity of the fornix and hippocampal atrophy, with fornix degeneration being a predictor of incipient cognitive decline in healthy elderly individuals[41]. However, it should also be noted that, although loss of WM integrity in the fornix is associated with cognitive decline and early AD pathology[39,44], only $K_\perp$ showed a significant decrease in this region of the 3xTg-AD mice. The fornix is a relatively small fiber tract adjacent to the ventricles, which makes it susceptible to partial volume effects of CSF. However, DK metrics are known to be less sensitive to CSF contamination[45] and we also mitigated this problem by masking out all voxels with MD $>$1.5 μm^2/ms.

Significant changes also occurred in other WM regions in the 3xTg-AD mice. Several diffusion measures (FA, $D_\parallel$, KFA, MK and $K_\perp$,) were significantly decreased, and $D_\perp$ was significantly increased in the corpus callosum, while DK metrics were significantly decreased in the internal and external capsule of these mice. A number of biological processes may underlie these dMRI changes seen in these WM tracts, including abnormal myelination and decrease in the density of myelinated axons, but a more comprehensive morphological characterization of different WM fibers in this model is needed to confirm the exact underlying mechanism for each region.

In several other mouse models of AD, dMRI has been used to detect WM changes associated with the presence of pathology in adult and older mice[46–51], but only a few dMRI studies have investigated WM abnormalities in this model. In older (11–17 months of age) 3xTg-AD mice Kastyak-Ibrahim et al.[24] reported no WM differences relative to controls using DTI, whereas our group, using DKI[25], demonstrated WM changes detected longitudinally, particularly in the fimbria and external capsule of 3xTg-AD mice (4.5 to 18 months of age). However, several methodological factors distinguish these two previous studies, including dMRI technique, gender differences for the mice, and ROIs sampling. In young 3xTg-AD mice, only one other MRI study has investigated WM abnormalities, reporting significant FA increase and $D_\perp$ decrease in the cortex and decrease hippocampal connectivity[26].

Although the expectations when studying animal models of AD at young age are that brain morphological changes will be minimal, the well-established alterations in myelination patterns described in young 3xTg-AD[17,18] and APP/PS1[52] mice supports the idea that myelin defects and oligodendrocyte dysfunction are early active contributors in the AD pathological process. While the mechanisms underlying reduced WM integrity in young 3xTg-AD are not totally clear, it has been suggested that early increases in Aβ peptide levels

and its cytotoxic effect on oligodendrocytes may be the trigger of myelin and oligodendrocyte defects[53]. Indeed, oligodendrocytes, the cells responsible for the production and maintenance of myelin, are very vulnerable to factors like oxidative stress, which impairs the differentiation of oligodendrocyte precursor cells or damage mature oligodendrocytes. Several studies suggest that Aβ-induced oxidative stress is toxic to oligodendrocytes[54,55], interfering with the myelination process and the ability to maintain existing myelin status, affecting axonal processes and making them vulnerable to disease-related processes, such as in AD[56,57].

Our results demonstrate that dMRI is a viable *in vivo* tool for assessing early WM pathology in AD. Several diffusion measures were able to capture significant widespread microstructural changes in WM fiber tracks in 2-month-old 3xTg-AD mice, which could represent a prodromal mechanistic feature related to AD pathology. Since our study focused on young 3xTg-AD mice, further studies will be needed to investigate the relationship between these early WM changes and AD pathology progression in this model. Additionally, since the myelin and oligodendrocyte defects can be reversed by inhibiting the release of Aβ-peptides[17] in this model, it is vital that future studies explore dMRI as a tool for detecting therapeutic effects in the 3xTg-AD mouse model. Lastly, because our dMRI methods are widely used and clinically-relevant in AD, our results have the potential to contribute to the further development of clinical neuroimaging biomarkers for both early detection and monitoring AD progression, which is crucial in the ongoing effort to find effective therapies to delay cognitive deficits.

5. Limitations

Our results should be considered in the context of some methodological limitations. First, because the voxels in our MRI acquisition were highly elongated, we could not reliably investigate the degree of connectivity between regions using fiber tracking analysis. Second, our ROI analysis approach limited the results to selected regions, precluding the measurement of differences throughout the entire brain. Additionally, in our ROI analysis we observed a significant difference in the size of hippocampus ROIs between groups, with smaller hippocampus ROIs being found the 3xTg-AD mice. However, this is consistent with the previously described small hippocampus volumes for the 3xTg-AD mouse model[28,29]. The ROI analysis approach was selected mainly because of these volume differences between the two groups (3xTg-AD and NC) would increase registration/normalization errors for the voxel-based analysis approach. Third, in our study, we applied Bonferroni corrections accounting for 8 dMRI metrics compared within each ROI, but not accounting for the total number of ROIs studied. There is no general consensus on how to apply the Bonferroni correction[58], and we choose this approach based on consistency with prior studies reporting dMRI results in mouse models of AD, including papers on the 3xTg-AD mouse[24,25]. Finally, the histological assessment was performed only on a small subset of mice (3xTg-AD, n = 9; NC, n = 5), for one histological marker (MBP – for myelin), and in only 2 slices at the level of the dorsal hippocampus. This limitation probably hindered our ability to detect differences in MBP immunoreactivity in brain regions other than fimbria. A more detailed morphological characterization with multiple morphological markers, labeling

oligodendrocytes and other glial cells, neurofilament, etc., with quantitative correlations between dMRI and morphology findings would be of interest.

6. Conclusion

In this study we have demonstrated, for the first time, that several dMRI measures are sensitive *in vivo* indicators of abnormalities in the brain cytoarchitecture of the 2-month-old 3xTg-AD mice, before they develop AD pathology. Significant differences, in comparison to NC mice, were detected in several brain regions, including the Fi, CC, and hippocampus. Thus, dMRI parameters may be useful as biomarkers for early detection of AD pathology, as well as for monitoring disease progression and effects of future therapeutic interventions. Since the dMRI methods employed here are easily translatable to clinical MRI, this study also demonstrates their potential for early detection of brain cytoarchitectural abnormalities in human AD patients.

Supplementary Material

Refer to Web version on PubMed Central for supplementary material.

Abbreviations:

AD	Alzheimer's disease
Aβ	amyloid beta
WM	white matter
DK	diffusional kurtosis
DKI	diffusional kurtosis imaging
DT	diffusion tensor
DTI	diffusion tensor imaging
FA	fractional anisotropy
MD	mean diffusivity
$D_{\parallel}$	axial diffusivity
$D_{\perp}$	radial diffusivity
KFA	kurtosis fractional anisotropy
MK	mean diffusional kurtosis
$K_{\parallel}$	axial kurtosis
$K_{\perp}$	radial kurtosis
Fi	fimbria

Fx	Fornix
EC	external capsule
IC	internal capsule
CC	corpus callosum
DH	dorsal hippocampus
VH	ventral hippocampus

References:

1. Braak H, Braak E. Neuropathological stageing of Alzheimer-related changes. Acta Neuropathol. 1991;82(4):239–259. [PubMed: 1759558]

2. Lam B, Masellis M, Freedman M, Stuss DT, Black SE. Clinical, imaging, and pathological heterogeneity of the Alzheimer's disease syndrome. Alzheimers Res Ther. 2013;5(1):1. [PubMed: 23302773]

3. Da Mesquita S, Ferreira AC, Sousa JC, Correia-Neves M, Sousa N, Marques F. Insights on the pathophysiology of Alzheimer's disease: The crosstalk between amyloid pathology, neuroinflammation and the peripheral immune system. Neuroscience and biobehavioral reviews. 2016;68:547–562. [PubMed: 27328788]

4. Brown WR, Thore CR. Review: cerebral microvascular pathology in ageing and neurodegeneration. Neuropathology and applied neurobiology. 2011;37(1):56–74. [PubMed: 20946471]

5. Pantoni L, Garcia JH. Cognitive impairment and cellular/vascular changes in the cerebral white matter. Annals of the New York Academy of Sciences. 1997;826:92–102. [PubMed: 9329683]

6. Bartzokis G, Sultzer D, Lu PH, Nuechterlein KH, Mintz J, Cummings JL. Heterogeneous age-related breakdown of white matter structural integrity: implications for cortical "disconnection" in aging and Alzheimer's disease. Neurobiology of aging. 2004;25(7):843–851. [PubMed: 15212838]

7. Banerjee K, Munshi S, Frank DE et al. Abnormal Glucose Metabolism in Alzheimer's Disease: Relation to Autophagy/Mitophagy and Therapeutic Approaches. Neurochem Res. 2015;40: 2557–2569. [PubMed: 26077923]

8. Theuring F, Thunecke M, Kosciessa U, Turner JD. Transgenic animals as models of neurodegenerative diseases in humans. Trends in biotechnology. 1997;15(8):320–325. [PubMed: 9263480]

9. Webster SJ, Bachstetter AD, Nelson PT, Schmitt FA, Van Eldik LJ. Using mice to model Alzheimer's dementia: an overview of the clinical disease and the preclinical behavioral changes in 10 mouse models. Frontiers in genetics. 2014; 5:88. [PubMed: 24795750]

10. Sterniczuk R, Dyck RH, Laferla FM, Antle MC. Characterization of the 3xTg-AD mouse model of Alzheimer's disease: part 1. Circadian changes. Brain research. 2010; 1348:139–148. [PubMed: 20471965]

11. Oddo S, Caccamo A, Shepherd JD, et al. Triple-transgenic model of Alzheimer's disease with plaques and tangles: intracellular Abeta and synaptic dysfunction. Neuron. 2003;39(3):409–421. [PubMed: 12895417]

12. Oddo S, Caccamo A, Kitazawa M, Tseng BP, LaFerla FM. Amyloid deposition precedes tangle formation in a triple transgenic model of Alzheimer's disease. Neurobiology of aging. 2003;24(8):1063–1070. [PubMed: 14643377]

13. Oddo S, Caccamo A, Tran L, et al. Temporal profile of amyloid-beta (Abeta) oligomerization in an in vivo model of Alzheimer disease. A link between Abeta and tau pathology. The Journal of biological chemistry. 2006;281(3):1599–1604. [PubMed: 16282321]

14. Belfiore R, Rodin A, Ferreira E, et al. Temporal and regional progression of Alzheimer's disease-like pathology in 3xTg-AD mice. Aging cell. 2019;18(1):e12873. [PubMed: 30488653]

15. Billings LM, Oddo S, Green KN, McGaugh JL, LaFerla FM. Intraneuronal Abeta causes the onset of early Alzheimer's disease-related cognitive deficits in transgenic mice. Neuron. 2005;45(5):675–688. [PubMed: 15748844]

16. Clark JK, Furgerson M, Crystal JD, Fechheimer M, Furukawa R, Wagner JJ. Alterations in synaptic plasticity coincide with deficits in spatial working memory in presymptomatic 3xTg-AD mice. Neurobiology of learning and memory. 2015;125:152–162. [PubMed: 26385257]

17. Desai MK, Mastrangelo MA, Ryan DA, Sudol KL, Narrow WC, Bowers WJ. Early oligodendrocyte/myelin pathology in Alzheimer's disease mice constitutes a novel therapeutic target. The American journal of pathology. 2010;177(3):1422–1435. [PubMed: 20696774]

18. Desai MK, Sudol KL, Janelsins MC, Mastrangelo MA, Frazer ME, Bowers WJ. Triple-transgenic Alzheimer's disease mice exhibit region-specific abnormalities in brain myelination patterns prior to appearance of amyloid and tau pathology. Glia. 2009;57(1):54–65. [PubMed: 18661556]

19. Abe O, Aoki S, Hayashi N, et al. Normal aging in the central nervous system: quantitative MR diffusion-tensor analysis. Neurobiology of aging. 2002;23(3):433–441. [PubMed: 11959406]

20. Stebbins GT, Murphy CM. Diffusion tensor imaging in Alzheimer's disease and mild cognitive impairment. Behav Neurol. 2009;21(1):39–49. [PubMed: 19847044]

21. Jensen JH, Helpern JA, Ramani A, Lu H, Kaczynski K. Diffusional kurtosis imaging: the quantification of non-gaussian water diffusion by means of magnetic resonance imaging. Magnetic resonance in medicine. 2005;53(6):1432–1440. [PubMed: 15906300]

22. Lu H, Jensen JH, Ramani A, Helpern JA. Three-dimensional characterization of non-gaussian water diffusion in humans using diffusion kurtosis imaging. NMR in biomedicine. 2006;19(2):236–247. [PubMed: 16521095]

23. Jensen JH, Helpern JA. MRI quantification of non-Gaussian water diffusion by kurtosis analysis. NMR in biomedicine. 2010;23(7):698–710. [PubMed: 20632416]

24. Kastyak-Ibrahim MZ, Di Curzio DL, Buist R, et al. Neurofibrillary tangles and plaques are not accompanied by white matter pathology in aged triple transgenic-Alzheimer disease mice. Magnetic resonance imaging. 2013;31(9):1515–1521. [PubMed: 23993791]

25. Nie X, Falangola MF, Ward R, et al. Diffusion MRI detects longitudinal white matter changes in the 3xTg-AD mouse model of Alzheimer's disease. Magnetic resonance imaging. 2019; 57:235–242. [PubMed: 30543850]

26. Manno FAM, Isla AG, Manno SHC, et al. Early Stage Alterations in White Matter and Decreased Functional Interhemispheric Hippocampal Connectivity in the 3xTg Mouse Model of Alzheimer's Disease. Frontiers in aging neuroscience. 2019; 11:39. [PubMed: 30967770]

27. Falangola MF, Nie X, McKinnon ET, Helpern JA, Jensen JH. Diffusion MRI detects changes in the Hippocampus and Fimbria-Fornix Circuit in 2 months old 3xTg-AD mice. Paper presented at: ISMRM 27th Annual Meeting; 15 May, 2019; Montréal, QC, Canada.

28. Kong V, Devenyi GA, Gallino D, et al. Early-in-life neuroanatomical and behavioural trajectories in a triple transgenic model of Alzheimer's disease. Brain structure & function. 2018;223(7):3365–3382. [PubMed: 29948190]

29. Chiquita S, Ribeiro M, Castelhano J, et al. A longitudinal multimodal in vivo molecular imaging study of the 3xTg-AD mouse model shows progressive early hippocampal and taurine loss. Human molecular genetics. 2019;28(13):2174–2188. [PubMed: 30816415]

30. Carroll JC, Rosario ER, Kreimer S, et al. Sex differences in beta-amyloid accumulation in 3xTg-AD mice: role of neonatal sex steroid hormone exposure. Brain research. 2010; 1366:233–245. [PubMed: 20934413]

31. Tabesh A, Jensen JH, Ardekani BA, Helpern JA. Estimation of tensors and tensor-derived measures in diffusional kurtosis imaging. Magnetic resonance in medicine. 2011;65(3):823–836. [PubMed: 21337412]

32. Veraart J, Novikov DS, Christiaens D, Ades-Aron B, Sijbers J, Fieremans E. Denoising of diffusion MRI using random matrix theory. NeuroImage. 2016; 142:394–406. [PubMed: 27523449]

33. Gudbjartsson H, Patz S. The Rician distribution of noisy MRI data. Magnetic resonance in medicine. 1995;34(6):910–914. [PubMed: 8598820]

34. Glenn GR, Helpern JA, Tabesh A, Jensen JH. Quantitative assessment of diffusional kurtosis anisotropy. NMR in biomedicine. 2015;28(4):448–459. [PubMed: 25728763]

35. Veraart J, Poot DH, Van Hecke W, et al. More accurate estimation of diffusion tensor parameters using diffusion Kurtosis imaging. Magnetic resonance in medicine. 2011;65(1):138–145. [PubMed: 20878760]

36. Schneider CA, Rasband WS, Eliceiri KW. NIH Image to ImageJ: 25 years of image analysis. Nature methods. 2012;9(7):671–675. [PubMed: 22930834]

37. Paxinos G, Franklin K. The Mouse Brain in Stereotaxic Coordinates. Compact 2nd ed: Elsevier Academic Press; 2004.

38. Bennett IJ, Huffman DJ, Stark CE. Limbic Tract Integrity Contributes to Pattern Separation Performance Across the Lifespan. Cereb Cortex. 2015;25(9):2988–2999. [PubMed: 24825784]

39. Kantarci K, Schwarz CG, Reid RI, et al. White matter integrity determined with diffusion tensor imaging in older adults without dementia: influence of amyloid load and neurodegeneration. JAMA neurology. 2014;71(12):1547–1554. [PubMed: 25347157]

40. Mielke MM, Okonkwo OC, Oishi K, et al. Fornix integrity and hippocampal volume predict memory decline and progression to Alzheimer's disease. Alzheimer's & dementia: the journal of the Alzheimer's Association. 2012;8(2):105–113.

41. Zhuang L, Wen W, Trollor JN, et al. Abnormalities of the fornix in mild cognitive impairment are related to episodic memory loss. Journal of Alzheimer's disease: JAD. 2012;29(3):629–639.

42. Amlien IK, Fjell AM. Diffusion tensor imaging of white matter degeneration in Alzheimer's disease and mild cognitive impairment. Neuroscience. 2014; 276:206–215. [PubMed: 24583036]

43. Rabin JS, Perea RD, Buckley RF, Johnson KA, Sperling RA, Hedden T. Synergism between fornix microstructure and beta amyloid accelerates memory decline in clinically normal older adults. Neurobiology of aging. 2019; 81:38–46. [PubMed: 31207468]

44. Dong JW, Jelescu IO, Ades-Aron B, et al. Diffusion MRI biomarkers of white matter microstructure vary nonmonotonically with increasing cerebral amyloid deposition. Neurobiology of aging. 2020.

45. Yang AW, Jensen JH, Hu CC, Tabesh A, Falangola MF, Helpern JA. Effect of cerebral spinal fluid suppression for diffusional kurtosis imaging. Journal of magnetic resonance imaging: JMRI. 2013;37(2):365–371. [PubMed: 23034866]

46. Sun SW, Song SK, Harms MP, et al. Detection of age-dependent brain injury in a mouse model of brain amyloidosis associated with Alzheimer's disease using magnetic resonance diffusion tensor imaging. Experimental neurology. 2005;191(1):77–85. [PubMed: 15589514]

47. Harms MP, Kotyk JJ, Merchant KM. Evaluation of white matter integrity in ex vivo brains of amyloid plaque- bearing APPsw transgenic mice using magnetic resonance diffusion tensor imaging. Experimental neurology. 2006;199(2):408–415. [PubMed: 16483571]

48. Shu X, Qin YY, Zhang S, et al. Voxel-based diffusion tensor imaging of an APP/PS1 mouse model of Alzheimer's disease. Molecular neurobiology. 2013;48(1):78–83. [PubMed: 23877934]

49. Vanhoutte G, Pereson S, Delgado YPR, et al. Diffusion kurtosis imaging to detect amyloidosis in an APP/PS1 mouse model for Alzheimer's disease. Magnetic resonance in medicine. 2013;69(4):1115–1121. [PubMed: 23494926]

50. Sahara N, Perez PD, Lin WL, et al. Age-related decline in white matter integrity in a mouse model of tauopathy: an in vivo diffusion tensor magnetic resonance imaging study. Neurobiology of aging. 2014;35(6):1364–1374. [PubMed: 24411290]

51. Badea A, Kane L, Anderson RJ, et al. The fornix provides multiple biomarkers to characterize circuit disruption in a mouse model of Alzheimer's disease. NeuroImage. 2016; 142:498–511. [PubMed: 27521741]

52. Wu Y, Ma Y, Liu Z, Geng Q, Chen Z, Zhang Y. Alterations of myelin morphology and oligodendrocyte development in early stage of Alzheimer's disease mouse model. Neuroscience letters. 2017; 642:102–106. [PubMed: 28174059]

53. Desai MK, Guercio BJ, Narrow WC, Bowers WJ. An Alzheimer's disease-relevant presenilin-1 mutation augments amyloid- beta-induced oligodendrocyte dysfunction. Glia. 2011;59(4):627–640. [PubMed: 21294162]

54. Smith MA, Rottkamp CA, Nunomura A, Raina AK, Perry G. Oxidative stress in Alzheimer's disease. Biochimica et biophysica acta. 2000;1502(1):139–144. [PubMed: 10899439]

55. Rottkamp CA, Nunomura A, Raina AK, Sayre LM, Perry G, Smith MA. Oxidative stress, antioxidants, and Alzheimer disease. Alzheimer disease and associated disorders. 2000;14 Suppl 1: S62–66. [PubMed: 10850732]

56. Bartzokis G, Tishler TA, Lu PH, et al. Brain ferritin iron may influence age- and gender-related risks of neurodegeneration. Neurobiology of aging. 2007;28(3):414–423. [PubMed: 16563566]

57. Nasrabady SE, Rizvi B, Goldman JE, Brickman AM. White matter changes in Alzheimer's disease: a focus on myelin and oligodendrocytes. Acta neuropathologica communications. 2018;6(1):22. [PubMed: 29499767]

58. Sjölander A, Vansteelandt S. Authors' reply to 'Multiple comparisons controversies are about context and costs, not frequentism versus Bayesianism'. Euro J Epidemiology. 2019;34:809–21.
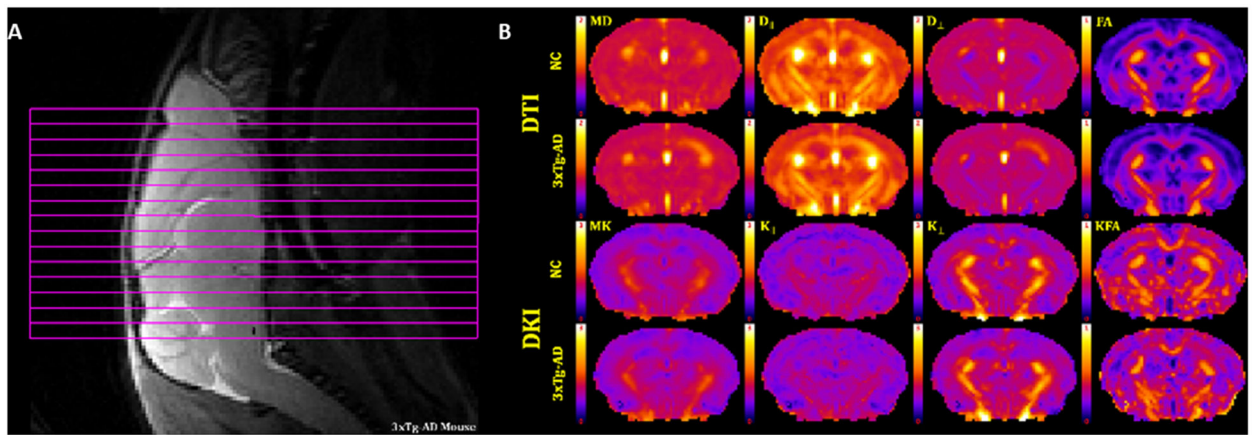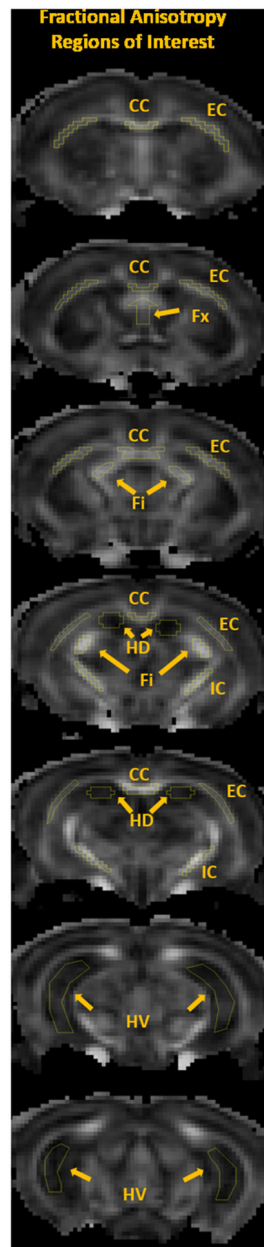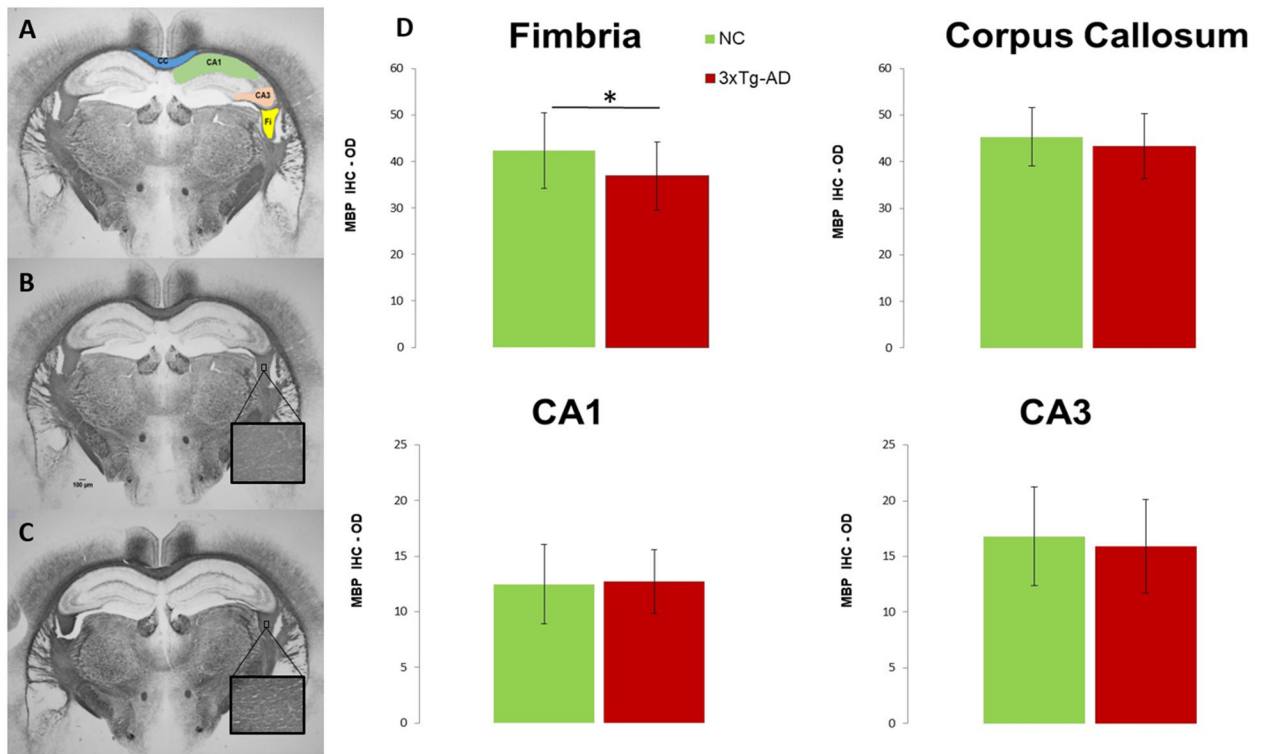
Figure 1.
(A) Slice positioning for the 15 coronal slices. **(B)** Representative dMRI parametric maps of all diffusion metrics, for a single anatomical slice, from a NC and a 3xTg-AD mouse. DT measures of mean diffusivity (MD), axial diffusivity ($D_{\parallel}$), radial diffusivity ($D_{\perp}$) and fractional anisotropy (FA). DK measures of mean kurtosis (MK), axial kurtosis ($K_{\parallel}$), radial kurtosis ($K_{\perp}$) and kurtosis fractional anisotropy (KFA). Scale bars: 0–1 for FA and KFA; 0–2 μm^2/ms for MD, $D_{\parallel}$ and $D_{\perp}$; 0–3 for MK, $K_{\parallel}$, and $K_{\perp}$.
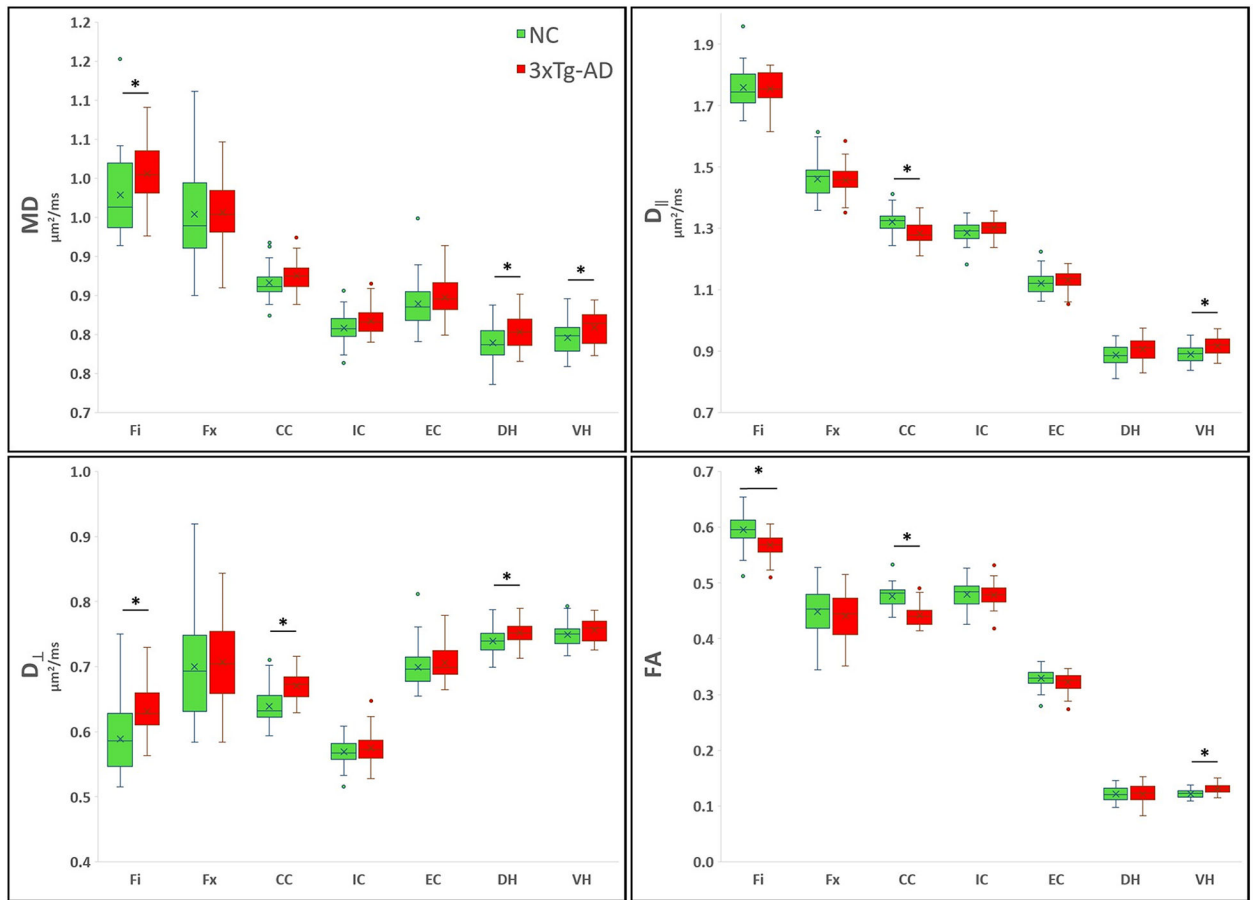
Figure 2:
Representative fractional anisotropy (FA) maps of a 2-month-old 3xTg-AD mouse illustrating the selected ROIs: corpus callosum (CC), external capsule (EC), fornix (Fx), fimbria (Fi), internal capsule (IC), dorsal hippocampus (DH) and ventral hippocampus (VH).
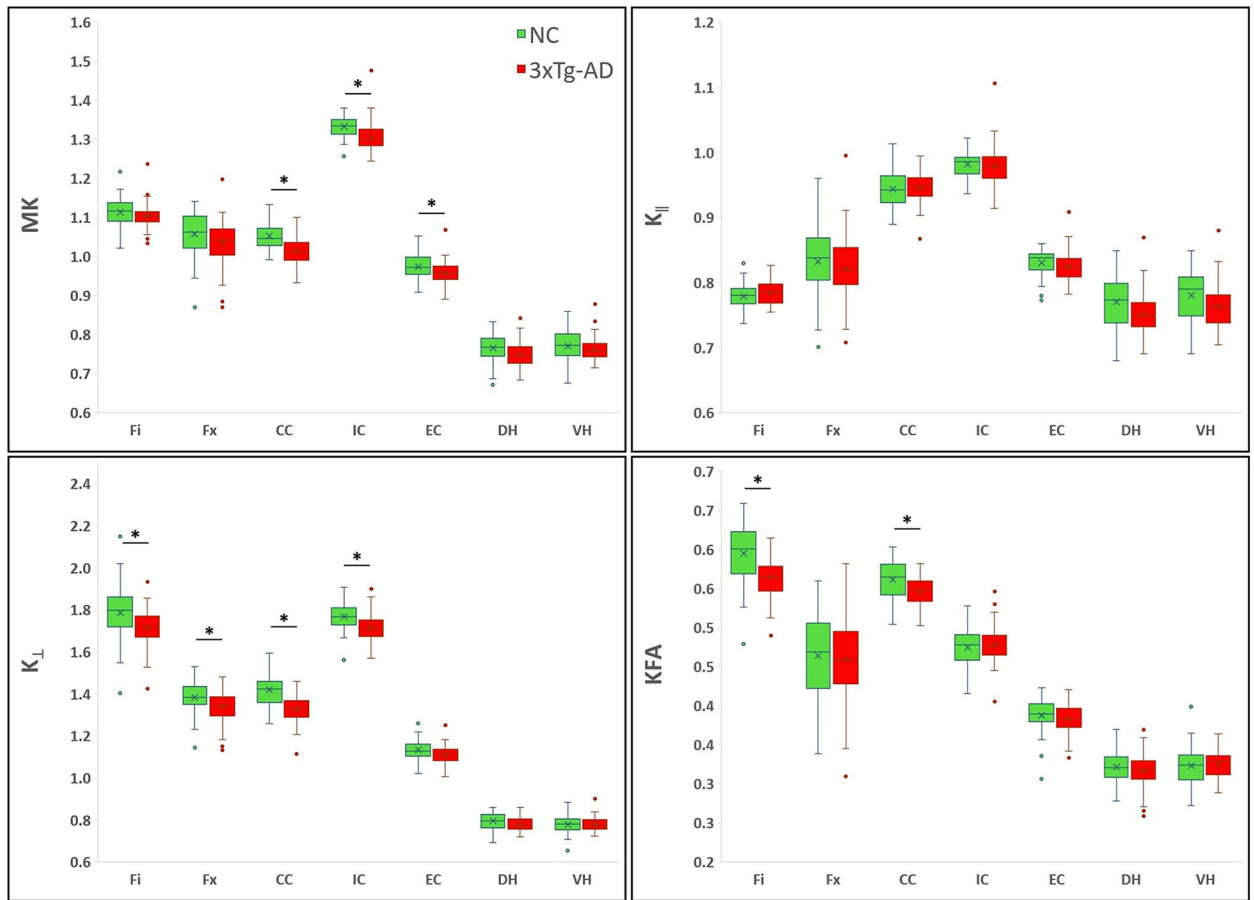
Figure 3:
(A) Representative of the myelin basic protein (MBP) stain (1.25x magnification) with ROIs highlighted for corpus callosum (CC), fimbria (Fi), and dorsal hippocampus subfields CA1 and CA3. Scale bar = 100μm. MBP stain for (B) 3xTg-AD and (C) NC mice (inserts 40x magnification). (D) Quantitative analysis of the MBP immunoreactivity; values are expressed as optical density (OD) = log (max intensity/mean intensity), where max intensity = 255 for the 8-bit images. * p   0.05.

Figure 4 -
Boxplots showing the averaged DT metrics. On the boxplots, data are presented as medians
(line), mean (x), quantile (box, 25–75% of data range), range (whiskers); outliers are
depicted with ovals dots. *indicates significant values for group comparison after Bonferroni
correction (8 dMRI comparisons).

Figure 5 -

Boxplots showing the averaged DK metrics. On the boxplots, data are presented as medians (line), mean (x), quantile (box, 25–75% of data range), range (whiskers); outliers are depicted with ovals dots. *indicates significant values for group comparison after Bonferroni correction (8 dMRI comparisons).

Table 1

DT metrics estimates (mean ± standard deviation, unadjusted p-values (bold indicates values that remain significant after Bonferroni correction for 8 dMRI comparisons), Cohen's d and the percentage differences for ROI. Mean (MD), axial (D$_\parallel$) and radial (D$_\perp$) diffusivities, fractional anisotropy (FA); fimbria (Fi), fornix (Fx), corpus callosum (CC), internal (IC) and external (EC) capsule, dorsal (DH) and ventral (VH) hippocampus.

		Mean (MD) Mean ± SD µm²/ms	Axial (D$_\parallel$) Mean ± SD µm²/ms	Radial (D$_\perp$) Mean ± SD µm²/ms	FA Mean ± SD
Fi	NC	0.979 ± 0.049	1.758 ± 0.062	0.589 ± 0.051	0.595 ± 0.027
	3xTg-AD	1.006 ± 0.036	1.755 ± 0.049	0.632 ± 0.038	0.568 ± 0.020
	p-values	**0.0031**	0.7898	**<.0001**	**<.0001**
	Cohen's d	0.655	−0.054	0.970	−1.206
	% Difference	2.800	−0.171	7.252	−4.621
Fx	NC	0.954 ± 0.061	1.462 ± 0.058	0.700 ± 0.079	0.449 ± 0.044
	3xTg-AD	0.957 ± 0.043	1.458 ± 0.047	0.706 ± 0.062	0.441 ± 0.042
	p-values	0.8025	0.679	0.6559	0.3607
	Cohen's d	0.054	−0.084	0.091	−0.187
	% Difference	0.294	−0.301	0.900	−1.761
CC	NC	0.866 ± 0.021	1.321 ± 0.037	0.639 ± 0.027	0.476 ± 0.020
	3xTg-AD	0.875 ± 0.019	1.285 ± 0.037	0.671 ± 0.021	0.441 ± 0.018
	p-values	0.0295	**<.0001**	**<.0001**	**<.0001**
	Cohen's d	0.449	−0.987	1.335	−1.865
	% Difference	1.016	−2.755	4.913	−7.389
IC	NC	0.808 ± 0.018	1.285 ± 0.036	0.570 ± 0.019	0.479 ± 0.021
	3xTg-AD	0.818 ± 0.017	1.303 ± 0.025	0.575 ± 0.021	0.479 ± 0.019
	p-values	0.0092	0.0091	0.203	0.9003
	Cohen's d	0.541	0.581	0.261	−0.026
	% Difference	1.163	1.362	0.930	−0.104
EC	NC	0.840 ± 0.029	1.121 ± 0.036	0.699 ± 0.030	0.329 ± 0.016
	3xTg-AD	0.848 ± 0.024	1.132 ± 0.030	0.706 ± 0.026	0.322 ± 0.016
	p-values	0.127	0.0928	0.2426	0.0418
	Cohen's d	0.313	0.345	0.239	−0.419
	% Difference	0.965	0.999	0.944	−2.037
DH	NC	0.789 ± 0.022	0.888 ± 0.033	0.740 ± 0.018	0.121 ± 0.012
	3xTg-AD	0.803 ± 0.022	0.906 ± 0.037	0.752 ± 0.016	0.122 ± 0.016
	p-values	**0.0019**	0.0125	**0.0006**	0.7775
	Cohen's d	0.648	0.517	0.720	0.058
	% Difference	1.774	2.050	1.622	0.741
VH	NC	0.796 ± 0.021	0.890 ± 0.027	0.749 ± 0.019	0.122 ± 0.007
	3xTg-AD	0.809 ± 0.020	0.916 ± 0.028	0.756 ± 0.017	0.131 ± 0.008
	p-values	**0.0022**	**<.0001**	0.0723	**<.0001**
	Cohen's d	0.639	0.948	0.369	1.129

	Mean (MD) Mean ± SD μm²/ms	Axial ($D_{\parallel}$) Mean ± SD μm²/ms	Radial ($D_{\perp}$) Mean ± SD μm²/ms	FA Mean ± SD
% Difference	1.633	2.932	0.854	7.201

Table 2

DK metrics estimates (mean ± standard deviation, unadjusted p-values (bold indicates values that remain significant after Bonferroni correction for 8 dMRI comparisons), Cohen's d and the percentage differences for ROI. Mean (MK), axial ($K_{\parallel}$), and radial ($K_{\perp}$) kurtoses and kurtosis fractional anisotropy (KFA); fimbria (Fi), fornix (Fx), corpus callosum (CC), internal (IC) and external (EC) capsule, dorsal (DH) and ventral (VH) hippocampus.

		Mean (MK)	Axial ($K_{\parallel}$)	Radial ($K_{\perp}$)	KFA
		Mean ± SD	Mean ± SD	Mean ± SD	Mean ± SD
Fi	NC	1.113 ± 0.041	0.779 ± 0.019	1.784 ± 0.132	0.595 ± 0.036
	3xTg-AD	1.102 ± 0.033	0.784 ± 0.019	1.711 ± 0.088	0.564 ± 0.025
	p-values	0.1437	0.1901	**0.0029**	**<.0001**
	Cohen's d	−0.300	0.268	−0.675	−1.026
	% Difference	−0.988	0.655	−4.091	−5.194
Fx	NC	1.058 ± 0.056	0.833 ± 0.055	1.384 ± 0.070	0.464 ± 0.052
	3xTg-AD	1.034 ± 0.055	0.821 ± 0.049	1.340 ± 0.080	0.459 ± 0.054
	p-values	0.0385	0.2841	**0.005**	0.6363
	Cohen's d	−0.427	−0.219	−0.584	−0.096
	% Difference	−2.241	−1.345	−3.194	−1.120
CC	NC	1.052 ± 0.032	0.943 ± 0.028	1.419 ± 0.074	0.562 ± 0.024
	3xTg-AD	1.015 ± 0.035	0.945 ± 0.024	1.328 ± 0.064	0.546 ± 0.020
	p-values	**<.0001**	0.7778	**<.0001**	**0.0005**
	Cohen's d	−1.099	0.058	−1.335	−0.730
	% Difference	−3.490	0.148	−6.426	−2.813
IC	NC	1.332 ± 0.027	0.982 ± 0.021	1.768 ± 0.062	0.474 ± 0.025
	3xTg-AD	1.307 ± 0.040	0.978 ± 0.030	1.714 ± 0.065	0.479 ± 0.023
	p-values	**0.0003**	0.4611	**<.0001**	0.343
	Cohen's d	−0.717	−0.142	−0.853	0.194
	% Difference	−1.907	−0.387	−3.088	0.991
EC	NC	0.974 ± 0.029	0.831 ± 0.021	1.132 ± 0.046	0.387 ± 0.024
	3xTg-AD	0.957 ± 0.028	0.824 ± 0.023	1.110 ± 0.041	0.383 ± 0.019
	p-values	**0.0034**	0.1779	0.0147	0.3080
	Cohen's d	−0.611	−0.276	−0.505	−0.208
	% Difference	−1.786	−0.746	−1.926	−1.136
DH	NC	0.766 ± 0.036	0.770 ± 0.040	0.794 ± 0.041	0.321 ± 0.020
	3xTg-AD	0.750 ± 0.031	0.752 ± 0.032	0.779 ± 0.033	0.317 ± 0.023
	p-values	0.0188	0.0136	0.0523	0.2567
	Cohen's d	−0.486	−0.511	−0.399	−0.232
	% Difference	−2.115	−2.376	−1.839	−1.525
VH	NC	0.771 ± 0.038	0.780 ± 0.041	0.778 ± 0.043	0.323 ± 0.025
	3xTg-AD	0.762 ± 0.031	0.764 ± 0.032	0.780 ± 0.033	0.324 ± 0.018
	p-values	0.1963	0.0398	0.8113	0.7242
	Cohen's d	−0.265	−0.424	0.051	0.076

	Mean (MK)	Axial (K$_\parallel$)	Radial (K$_\perp$)	KFA
	Mean ± SD	Mean ± SD	Mean ± SD	Mean ± SD
% Difference	−1.154	−1.975	0.257	0.496